Dalton Transactions

ROYAL SOCIETY OF CHEMISTRY

PAPER

View Article Online
View Journal | View Issue

Cite this: *Dalton Trans.*, 2024, **53**, 11147

$Ti_3C_2T_x$ MXene reinforcement: a nickel–vanadium selenide/MXene based multi-component composite as a battery-type electrode for supercapacitor applications†

Khadija Chaudhary, [a] Sonia Zulfiqar, [b,c] Khamael M. Abualnaja,[d] Muhammad Shahid,[e] Hala M. Abo-Dief,[f] Muhammad Farooq Warsi *[a] and Eric W. Cochran *[c]

Designing innovative microstructures and implementing efficient multicomponent strategies are still challenging to achieve high-performance and chemo-mechanically stable electrode materials. Herein, a hierarchical three-dimensional (3D) graphene oxide (GO) assisted $Ti_3C_2T_x$ MXene aerogel foam (MXene-GAF) impregnated with battery-type bimetallic nickel vanadium selenide (NiVSe) has been prepared through a hydrothermal method followed by freeze-drying (denoted as NiVSe–MXene-GAF). 3D-oriented cellular pore networks benefit the energy storage process through the effective lodging of NiVSe particles, improving the access of the electrolyte to the active sites, and alleviating volume changes during redox reactions. The 3D MXene-GAF conductive matrix and heterostructured interface of MXene–rGO and NiVSe facilitated the rapid transport of electrical charges and ions during the charge–discharge process. As a result of the synergism of these effects, NiVSe–MXene-GAF exhibited remarkable electrochemical performance with a specific capacity of 305.8 mA h g^{-1} at 1 A g^{-1} and 99.2% initial coulombic efficiency. The NiVSe–MXene-GAF electrode delivered a specific capacity of 235.1 mA h g^{-1} even at a high current density of 12 A g^{-1} with a 76.8% rate performance. The impedance measurements indicated a low bulk solution resistance (R_s = 0.71 Ω) for NiVSe–MXene-GAF. Furthermore, the structural robustness of NiVSe–MXene-GAF guaranteed long-term stability with a 91.7% capacity retention for successive 7000 cycles. Thus, developing NiVSe–MXene-GAF provides a progressive strategy for fabricating high-performance 3D heterostructured electrode materials for energy storage applications.

Received 25th April 2024,
Accepted 5th June 2024

DOI: 10.1039/d4dt01230e

rsc.li/dalton

1. Introduction

The interest in electrochemical energy storage is constantly increasing and is mainly driven by the motives to utilize inexhaustible renewable energy and decarbonize the industrial sectors.[1] Due to their extraordinary performance characteristics, *i.e.*, high power density, long cyclic life, and fast charge–discharge rates, supercapacitors can be considered the device of choice for future electrochemical energy storage systems.[2,3] When considering an electrode for an efficient energy storage device, it must satisfy the requirement for high energy density, along with the aforementioned performance characteristics.[4,5] Based on the energy storage mechanism, supercapacitor electrode materials can be classified as pseudocapacitor electrode (PC) materials, electrical double-layer capacitor (EDLC) electrode materials, and battery-type electrode materials.[6] Due to the high theoretical capacity originating from the enormous redox activity, battery-type electrode materials are gaining special interest among researchers.[7]

[a]*Institute of Chemistry, Baghdad-ul-Jadeed Campus, The Islamia University of Bahawalpur, Bahawalpur-63100, Pakistan. E-mail: farooq.warsi@iub.edu.pk*
[b]*Department of Chemistry, Faculty of Science, University of Ostrava, 30. Dubna 22, Ostrava, 701 03, Czech Republic*
[c]*Department of Chemical and Biological Engineering, Iowa State University, Sweeney Hall, 618 Bissell Road, Ames, Iowa, 50011, USA. E-mail: ecochran@iastate.edu*
[d]*Department of Chemistry, College of Science, Taif University, P. O. Box 11099, Taif, 21944, Saudi Arabia*
[e]*Department of Chemistry, College of Science, University of Hafr Al Batin, P. O. Box 1803, Hafr Al Batin, 31991, Saudi Arabia*
[f]*Department of Science and Technology, University College-Ranyah, Taif University, P. O. Box 11099, Taif 21944, Saudi Arabia*

† Electronic supplementary information (ESI) available: XRD patterns, FT-IR and UV-vis spectra of GO (Fig. S1), FT-IR and UV-vis spectra of MXenes (Fig. S2), and specific capacity of NiVSe, NiVSe-GAF, and NiVSe–MXene-GAF at different current densities (Table S1). See DOI: https://doi.org/10.1039/d4dt01230e

Lately, transition metal selenides have gained significant attention as battery-type electrodes due to their enriched active sites, high electrical conductivity, low band gap, and remarkable specific capacity compared to their oxide/hydroxide analogs.[8–10] To date, a number of metal selenides such as nickel selenide,[11] iron selenide,[12] cobalt selenide,[13] and vanadium selenide[14] have been exploited as supercapacitor electrode materials. In addition to monometallic selenides, the use of bimetallic alloys has been shown to discover novel functions such as unprecedented synergistic effects, enhanced electrochemical activity, and modified electronic structures. For instance, Xie *et al.* studied the alloying effect for bimetallic $Ni_xCo_{1-x}Se_2$.[15] The as-prepared electrode showed a high specific capacitance of 1580 F g^{-1} at 1 A g^{-1} which was greater than those of its monometallic $NiSe_2$ and $CoSe_2$ constituents. In another report, Moosavifard *et al.* synthesized bimetallic CuCoSe hollow structures using a solvothermal method, and the resulting materials exhibited a considerable specific capacity of 562 C g^{-1} at 2 A g^{-1}.[16] Liu *et al.* prepared Ni–Co–Se core–shell spheres using the hydrothermal method followed by selenization.[17] The prepared supercapacitor electrode material exhibited a specific capacity of 164.4 mA h g^{-1} at 1 A g^{-1}. Still, despite the capability to offer significant energy storage, volume changes and pulverization of the battery-type material during electrochemical reactions affect the cycling life and rate capability of the electrode leading to underperformance, especially at high current densities.[18,19] Additionally, due to the inefficient use of active sites (*i.e.* dead mass that is not accessible to electrolyte ions for electrochemical reaction) transition metal selenides cannot reach their maximum activity and still face limitations in terms of energy storage.[20] To circumvent these problems, optimization of the electrode architecture in terms of fast and facile access of electrolyte ions to the active centers and structural integrity has become imperative.

A carbon-based aerogel architecture can act as a robust host for the active material due to the open porous network and three-dimensional (3D) interlinked pathways as ionic and electronic channels for operative charge–discharge. Recently, Park and co-workers loaded $Fe_{1-x}S$ in a 3D reduced graphene oxide (rGO) aerogel.[21] The as-obtained $Fe_{1-x}S$/rGOA composite electrode attained a high specific capacitance of 643 F g^{-1} at 1 A g^{-1} and retained 399.3 F g^{-1} of capacitance even at a very fast charge–discharge rate of 10 A g^{-1}. Similarly, Zhou *et al.* developed a biomass-derived MnO_x/carbon aerogel showing 557 F g^{-1} of specific capacitance and nearly 50% capacitance retention up to 10 000 CV cycles.[22] A carboxymethyl cellulose-derived carbon aerogel/NiO composite exhibited excellent electrochemical stability and a high specific capacity of 81.67 mA h g^{-1} at 0.5 A g^{-1}.[23] Similarly, Ranjbar *et al.* reported a crosslinked graphene aerogel embedded Fe_2O_3 composite (CL-GA/Fe_2O_3). The specific capacitance of CL-GA/Fe_2O_3 (445 F g^{-1}) surpassed that of Fe_2O_3 (150 F g^{-1}) with 89% capacitance retention after 5000 cycles.[24]

In the family of carbon-based composites for energy storage, $Ti_3C_2T_x$ (T_x = –F, –OH, –O) MXenes are emerging as advanced futuristic materials as they are effective supports for active materials. The high conductivity (up to 14 000 S cm^{-1}), large surface area, pseudocapacitive behavior, and intrinsic hydrophilic character of $Ti_3C_2T_x$ MXenes work in synergy with the active material to enhance the electrochemical activity.[25–27] However, it is difficult to assemble $Ti_3C_2T_x$ MXenes into an aerogel framework due to the tough-nature and small size of $Ti_3C_2T_x$ MXene films. However, by adjusting a certain amount of graphene oxide (GO) as a gelation agent with the $Ti_3C_2T_x$ MXene, a stable $Ti_3C_2T_x$ MXene–rGO hydrogel can be obtained that can be later on transformed into an aerogel.[28] In addition to aiding the assembly of 3D monoliths, rGO contributes to the flexibility and mechanical strength of the structure while also providing an enhanced surface area and electrical conductivity, thereby amplifying the synergistic effects of the aerogel.[26,29,30] Hitherto, some GO-based $Ti_3C_2T_x$ MXene aerogels such as S,N–rGO@MXene,[31] MXene/rGOAMs,[32] $Ti_3C_2T_x$/rGO/Fe_3O_4,[33] $Ti_3C_2T_x$ MXene/rGO/SnO_2 [34] and MXene/rGO/CuO [35] have been prepared and reported for electrochemical applications. Yet, the impregnation of bimetallic selenides in $Ti_3C_2T_x$ MXene-based aerogels is seldom reported in the literature.

Herein, bimetallic nickel vanadium selenide (NiVSe) has been prepared and integrated into GO-assisted $Ti_3C_2T_x$ MXene (hereafter denoted as MXene) aerogel foam (MXene-GAF) through hydrothermal and freeze drying methods. Battery-type bimetallic NiVSe delivered rich redox active sites for electrochemical reactions. The high electrical conductivity of the MXene, coupled with rGO, facilitated rapid charge and ionic transport. The 3D open porous network of aerogel foam and heterostructured surface formed by MXene–rGO and NiVSe significantly improved the accessibility of the electrolyte to the active sites. Simultaneously, the 3D hierarchical framework, flexibility of rGO sheets, and potent interaction among the individual components offered chemo-mechanical stability to the electrode. As a result, as the designed NiVSe–MXene-GAF electrode exhibits high specific capacity, rate capability, and cycling stability. Ultimately, this work presents a useful strategy to develop 3D hierarchical and multicomponent electrode materials for high performance energy storage devices.

2. Experimental section

2.1. Materials

Ammonium metavanadate (NH_4VO_3); ≥99.0%, nickel chloride ($NiCl_2{\cdot}6H_2O$); 99.9% trace metals basis, urea ($CO(NH_2)_2$); 99.0–100.5%, ammonium fluoride (NH_4F); ≥98.0%, selenium powder (Se); 99.99% trace metals basis, sodium hydroxide (NaOH); ≥97.0%, pellets, graphite flakes; 99% carbon basis, −325 mesh particle size (≥99%), sulfuric acid (H_2SO_4); 95–98%, sodium nitrate ($NaNO_3$); ≥99.0%, hydrogen peroxide (H_2O_2); 30% (w/w) in H_2O, MAX powder (Ti_3AlC_2); ≥90%, ≤200 μm particle size, and hydrofluoric acid (HF); 48% were used during the synthesis of materials. All chemicals were procured from Sigma Aldrich.

2.2. Synthesis of NiVSe

Synthesis of NiVSe was carried out using a two-step hydrothermal method. In the first step, a NiV-layered double hydroxide (LDH) precursor was prepared. For this, NH_4VO_3 (0.2 mmol), $NiCl_2{\cdot}6H_2O$ (0.6 mmol), $CO(NH_2)_2$ (3.3 mmol), and NH_4F (2.6 mmol) were added in 40 mL of distilled water and stirred for 15 min. The resulting solution was transferred into 50 mL of autoclave and incubated at 180 °C for 6 h. After the completion of the reaction, precipitates were removed from the solution and washed with ethanol and water successively. Precipitates were dried at 60 °C to finally obtain NiV LDH. In the second step, Se powder (3.9 mmol) and NaOH (0.046 mol) were added to 80 mL of distilled water. The solution was stirred at 90 °C for 12 h to obtain Na_2SeO_3. The NiV LDH precursor was added to freshly prepared Na_2SeO_3, and the solution was stirred for 30 min. Next, the solution was transferred into an autoclave and treated at 180 °C for 9 h. Finally, the product precipitates were removed from the autoclave, washed with ethanol/distilled water and dried at 60 °C to obtain NiVSe.

2.3. Synthesis of GO and MXene dispersion

Graphene oxide (GO) was prepared through the Hummers' method mentioned in detail in our previous report.[36] For the synthesis of MXene, 20 mL of HF was taken in a plastic reaction tube and 1 g of Ti_3AlC_2 powder was slowly added to the etching solution for 1 min. The reaction was maintained under constant stirring conditions at 35 °C for 24 h. Afterward, the precipitates were washed with distilled water several times until a pH of around 7 was obtained. Next, the as-obtained precipitates were added to 100 mL of distilled water and ultrasonicated for 30 min, and then dried at 60 °C to obtain exfoliated MXene sheets. Fig. S1 and S2† provide the characterization for as-synthesized GO and MXene.

2.4. Assembly of NiVSe–MXene-GAF

For the assembly of NiVSe–MXene-GAF, 50 mg of NiVSe was added into 40 mL of MXene : GO (1 : 1.5) dispersion in distilled water. The mixture was ultrasonicated (power = 200 W) for 30 min to obtain a stable suspension. Afterward, 20 mg of ascorbic acid was added to the homogeneous suspension under stirring conditions for 5 min. Next, the suspension was transferred to a 50 mL autoclave and the reaction was set at 70 °C for 4 h. After the completion of the reaction, a 3D hydrogel monolith was separated from the solvent and freeze-dried at −90 °C to obtain NiVSe–MXene-GAF (Fig. 1). In addition to NiVSe–MXene-GAF, NiVSe-GAF was also prepared by following the same procedure except with the addition of MXene during the first step.

2.5. Characterization and electrochemical measurements

Morphological and elemental studies of the prepared materials were carried out using a Hitachi SU4800 FE-SEM field emission scanning electron microscope. Phase studies were performed on a Philips X'Pert X-ray diffractometer. The chemical composition of materials was determined through XPS analysis using a Kratos Amicus/ESCA 3400 instrument. Shimadzu FT-IR affinity/1S was used for the functional analysis. Thermal stability of the materials was analyzed through TGA analysis on a Shimadzu TGA-50 thermogravimetric analyzer. To determine the DC conductivity current–voltage measurements were carried out on a picoammeter Keithley-2450 source meter. To investigate the electrochemical performance of our prepared materials, cyclic voltammetry (CV), galvanostatic charge–discharge (GCD), and electrochemical impe-

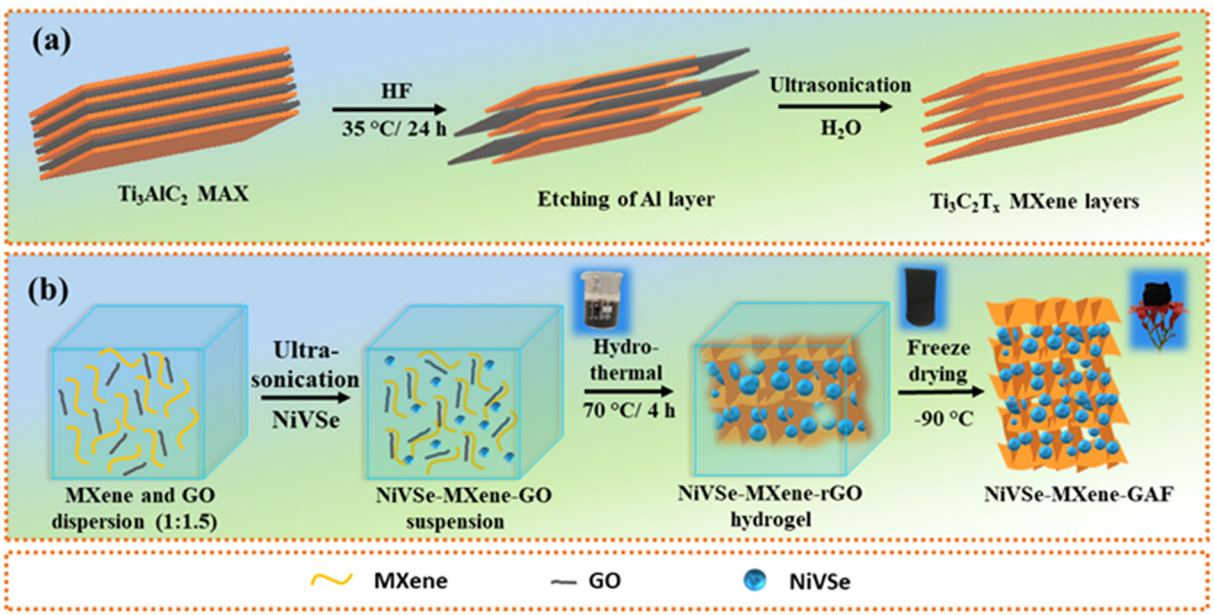

Fig. 1 Schematic illustration of (a) the synthesis of the MXene and (b) assembly of NiVSe–MXene-GAF.

dance spectroscopy (EIS) measurements were conducted on an interface 5000E Potentiostat from GAMRY instruments. For this, the working electrode was prepared by compressing the aerogel foams (NiVSe-GAF and NiVSe–MXene-GAF) within two pieces of Ni-foam (2×1 cm^2) with the help of a hydraulic press (with a total weight loading of 3 mg). For pure NiVSe, a working electrode was prepared using a drop-casting method using a homogeneous ink solution of active material. The homogeneous ink was prepared by mixing an appropriate amount of NiVSe with 50 μL of Nafion (5 wt%) binder, and 1 mL of ethanol. An electrode system comprised of Ag/AgCl (reference electrode), a ~4 cm long Pt-wire (auxiliary electrode), and Ni-foam deposited active material was used as the half-cell for the supercapacitor study. All the electrochemical measurements were conducted using a 3 M KOH electrolyte solution.

3. Results and discussion

3.1. Morphological and elemental analyses

The morphological features of the prepared materials were comprehensively analyzed through FESEM. As shown in Fig. 1 (a and b), NiVSe exhibits the morphology of asymmetric particles. Fig. 2(c) represents 2D MXene layers (lateral size 8.09 μm) with the clearly visible interlayer spacing introduced after the etching and exfoliation of the MAX phase. Whereas, pure MXene-GAF exhibits a 3D structure in Fig. 2(d) where MXene–rGO nanosheets crosslink with each other to form a hierarchical aerogel foam. As can be seen, the aerogel foam is composed of multiple cellular units of variable cell widths. In fact, during the hydrothermal process, the crosslinking phenomenon generates the primary porous entities in the hydrogel monolith.[37] Later on, during the freeze drying, as the ice crystals grow they break through the weakly crosslinked nanosheets and induce a modular effect which results in larger cellular units. In comparison with MXene-GAF, NiVSe particles can be seen through the aerogel foams in NiVSe-GAF (Fig. 2(e and f)) and NiVSe–MXene-GAF (Fig. 2(g and h)). Apparently, the addition of NiVSe affects the regular construction of cellular units (high magnification images in Fig. 2(f and h)), yet the 3D crosslinked porous structure of aerogel foams persists in NiVSe-GAF and NiVSe–MXene-GAF. Similar observations were made by Cai *et al.* for MXene/graphene oxide/Co_3O_4 aerogels.[38] Nonetheless, the highly porous 3D skeleton is beneficial for multi-dimensional ion diffusion and thereby it will improve the accessibility of electrolyte ions to NiVSe active sites. In addition, the 3D buildup of MXene-GAF prevents the stacking of MXene–rGO sheets and random aggregation of NiVSe nanoparticles.

The EDX spectra of NiVSe, NiVSe-GAF, and NiVSe–MXene-GAF are shown in Fig. 3(a–c). Pure NiVSe (Fig. 3(a)) exhibits peaks from the different energy levels of Ni (0.85 keV and 7.4 keV), V (0.51 keV and 4.94 keV), and Se (1.37 keV). For NiVSe-GAF (Fig. 3(b)), two new peaks were observed at 0.27 keV and 0.53 keV from C and O elements due to the rGO content. Whereas, NiVSe–MXene-GAF (Fig. 3(c)) accumulates all former elements (Ni, V, Se, C, and O) with Ti at 0.45 keV and 4.5 keV. Notably, the ratio of C/Ti is high in NiVSe–MXene-GAF (Fig. 3(c)) which is due to the extra C from rGO which confirms the amalgamation of MXene with rGO.

3.2. Phase analysis

For phase identification and crystal structure analysis, XRD studies were carried out for the synthesized materials, as shown in Fig. 4(a). XRD pattern of MXene displays characteristic diffraction planes (002), (006), (008), (103), (105), (110), (201), and (202) at 2θ = 8.4°, 18.2°, 25°, 36.1°, 41.7°, 60.7°, 72.6°, and 76.5°, respectively (JCPDS: 52-0875). The absence of the (104) peak (at 38.7°) in MXene in contrast to the MAX phase confirms the removal of the Al-layer. For NiVSe, XRD peaks at 29.5°, 39°, 62.3°, and 76.5° correspond to (012), (211), (024), and (401) planes of monoclinic Ni_2Se_3 (JCPDS: 18-0890). Peaks located at 34.1° and 43.9° are indexed to (011) and (102) planes of hexagonal VSe_2 (JCPDS: 89-1641). Furthermore, prominent peaks at 52.2° and 61.9° well matches with (040) and (317) planes of monoclinic V_5Se_8 (JCPDS: 18-1455). This triphase composition of NiVSe will provide rich redox chemistry to bimetallic alloy for electrochemical energy storage.[39] The broad peak in NiVSe-GAF and NiVSe–MXene-GAF at ~23.8° is arised from the graphitic structure of rGO. Presence of this broad peak at a high value of 2θ (in comparison with a sharp peak of GO at 10.3 [40]) implies the reduction of GO sheets during the construction of aerogel foam. A sharp peak at 7.7° in NiVSe–MXene-GAF is assigned to the characteristic (002) plane of MXene. A peak shift for MXene from 8.4° to 7.7° (for 002 plane) is a manifestation of the increase in the interlayer spacing of MXene layers after its assembly into aerogel foam. Moreover, a partial magnification of the XRD pattern in Fig. 4(b) indicates a peak shift and peak expansion for NiVSe in aerogel foams, and the effect is maximum for NiVSe–MXene-GAF. These changes in the features of the XRD pattern are assignable to the variations in the lattice parameters or lattice strain after the integration of NiVSe into NiVSe-GAF and NiVSe–MXene-GAF heterostructures. Regardless, the presence of distinctive diffraction peaks from the corresponding components substantiates that NiVSe–MXene-GAF is a hybrid of NiVSe, MXene, and rGO.

3.3. Functional group analysis

FT-IR analysis was used to investigate the characteristic functional groups within NiVSe, NiVSe-GAF, and NiVSe–MXene-GAF. FT-IR spectra depicted in Fig. 5 exhibit discernable bands below 1000 cm^{-1} assignable to various metal–selenide (M–Se) bond vibrations in bimetallic NiVSe. Specifically, bands observed at 455, 745, and 831 cm^{-1} correspond to different vibrational modes arising from the Ni–Se bond.[41] The bands at 515 and 954 cm^{-1} are ascribed to V–Se bond vibrations.[42] Besides the M–Se bonds, a broad band at around 3393 cm^{-1} and a narrow band at 1636 cm^{-1} are assigned to O–H stretching and bending vibrations, respectively, which are contributed by strongly coordinated water molecules.[43] When NiVSe is integrated into aerogel foams, numerous new bands appeared

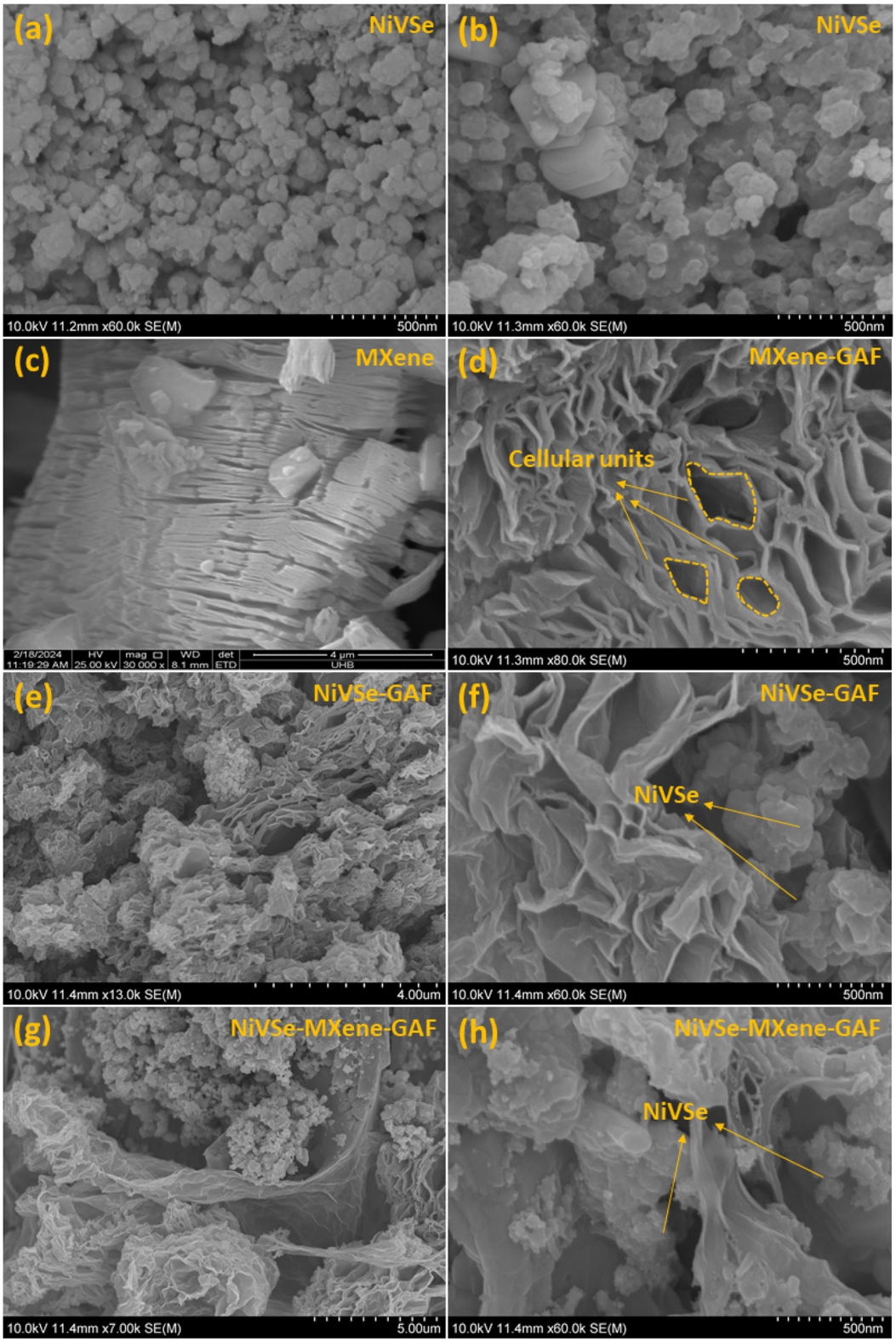

Fig. 2 FESEM images: (a and b) NiVSe, (c) MXene, (d) MXene-GAF, (e and f) NiVSe-GAF, and (g–h) NiVSe–MXene-GAF.

within the range of 1000–1800 cm^{-1} due to the surface moieties located over MXene and rGO sheets, and graphitic contents of the rGO skeleton. A prominent band at 1554 cm^{-1} is contributed by aromatic C=C stretching in the rGO and plausibly arise due to the restoration of the conjugated structure after the hydrothermal reduction of GO.[44] As the reduction is

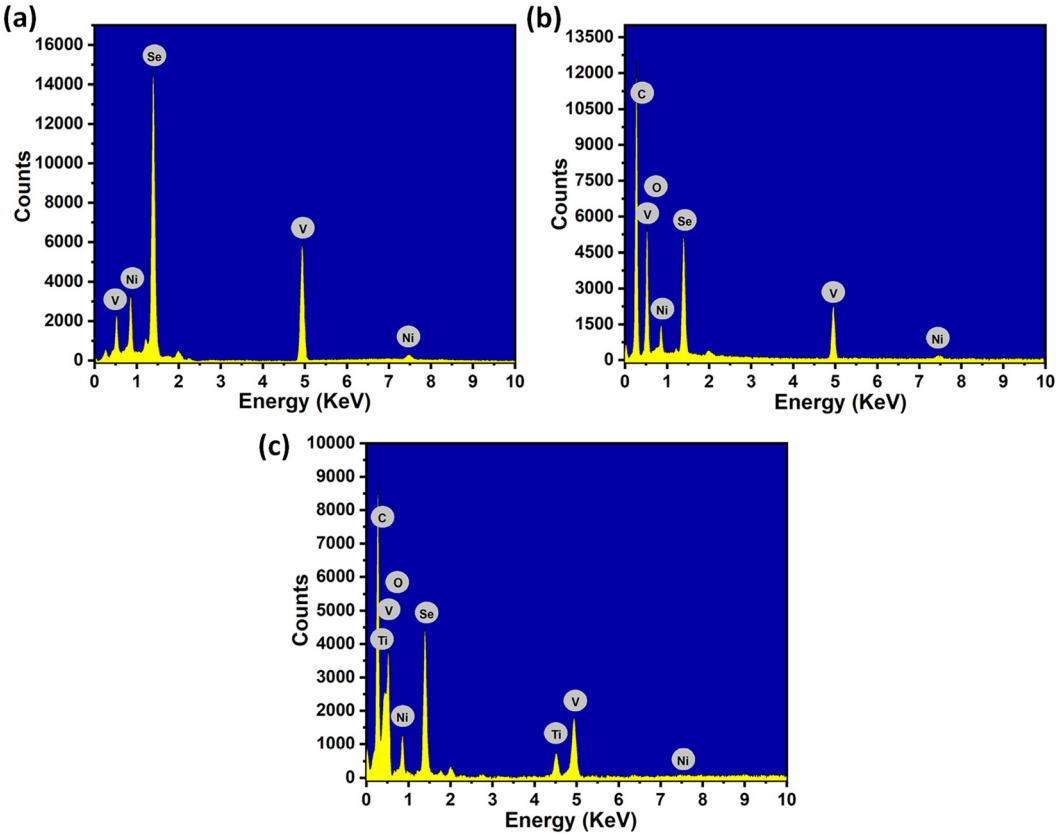

Fig. 3 EDX spectra of (a) NiVSe, (b) NiVSe-GAF, and (b) NiVSe–MXene-GAF.

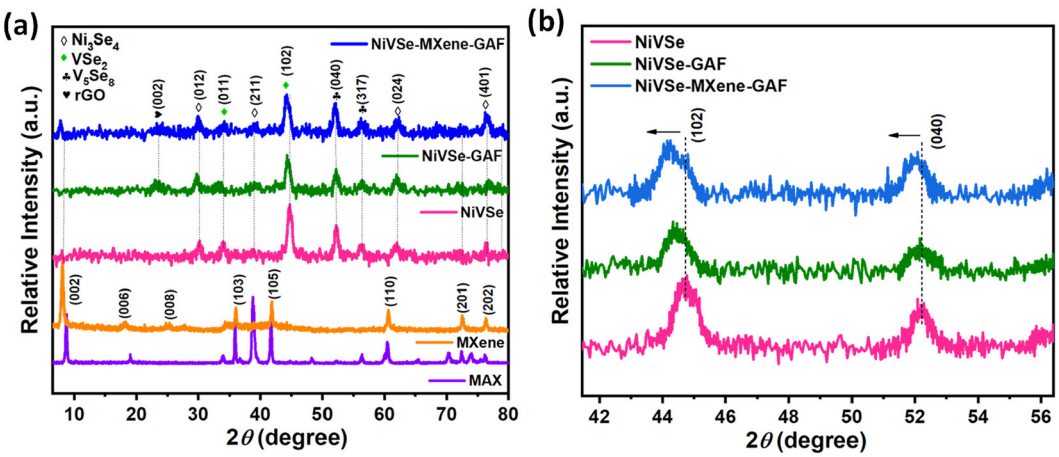

Fig. 4 (a) XRD patterns of MAX, MXene, NiVSe, NiVSe-GAF, and NiVSe–MXene-GAF and (b) peak shift indicated by the partial magnification of the XRD pattern for NiVSe, NiVSe-GAF, and NiVSe–MXene-GAF.

only partial, the oxygen containing moieties in the form of epoxy C–O–C and carboxyl C═O groups can be observed at 1096 and 1718 cm^{-1}, respectively.[45,46] Additionally, the –OH bending and C–O stretching vibrations in –COOH are observed at 1390 and 1245 cm^{-1}, respectively.[46] It is noteworthy that both NiVSe-GAF and NiVSe–MXene-GAF show similar bands in the functional group region, the intensity of bands is relatively high for NiVSe–MXene-GAF. This increase in the band's intensity can be ascribed to the incorporation of additional oxygen-containing functionalities from MXene, giving NiVSe–MXene-GAF a more hydrophilic character as evident from the intense O–H band. It is well reported that the C–F terminations in HF etched MXene are observed in the range of ~1072–1375.[47] Therefore, mixed oxygen/fluorine terminations can be

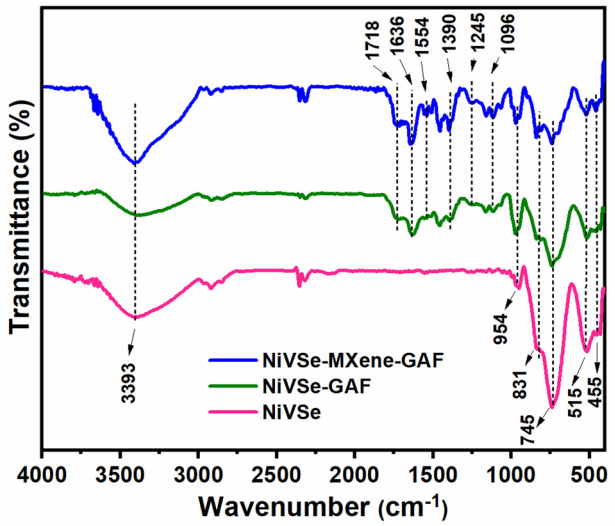

Fig. 5 FT-IR spectra of NiVSe, NiVSe-GAF and NiVSe–MXene-GAF.

expected in this range in the FT-IR spectrum of NiVSe–MXene-GAF. The functional groups (–C–O–C, –COOH, –OH, and –F) on the surface of aerogel foams interact (through van der Waals forces and/or covalent bond interactions) with NiVSe and act as anchoring sites for these particles. These interactions among NiVSe and MXene-GAF bridge conductive channels between them and facilitate charge transfer during the electrochemical process.[48]

Also, as reported by Li *et al.* an upshift in the O–H band from 3367 cm^{-1} to 3405 cm^{-1} in NiVSe–MXene-GAF as compared to NiVSe-GAF indicates the existence of H-bonding that plays a vital role during the assembly of MXene-GAF.[49]

3.4. XPS analysis

In order to further understand the chemical bonding and chemical composition of materials, XPS analysis was carried out and the results are presented in Fig. 6(a–f). The high-resolution XPS spectrum of Ni 2p shows two pairs of Ni $2p_{3/2}$ and Ni $2p_{1/2}$ and the corresponding satellite peaks. Peaks at 857.2 and 874.1 eV are assigned to the Ni^{2+} oxidation state corresponding to Ni–Se in NiVSe (Fig. 6(a)).[50] The peaks located at 872.3 and 854.7 eV originate from Ni^{3+}.[51] Similarly, V 2p peaks are deconvoluted to V $2p_{1/2}$ and V $2p_{3/2}$ doublet core energy levels with peaks at 524 and 516.7 eV for V^{4+} in V–Se of NiVSe (Fig. 6(b)).[52] Second pair of peaks with binding energies at 521.9 and 514.3 eV correspond to V^{5+}.[53] The deconvoluted spectra of Ni 2p and V 2p show the existence of Ni^{3+} and V^{5+} which originated from the surface oxides formed during the hydrothermal synthesis.[51] Deconvoluted peaks in the high resolution XPS spectrum of Se 3d at the binding energies of 53.8 and 55.4 eV are ascribed to Se $3d_{5/2}$ and Se $3d_{3/2}$ energy levels (Fig. 6(c)).[50] The high resolution XPS spectrum of Ti 2p shows the existence of the Ti–C bond at the binding energies of 459.6 and 454 eV (Fig. 6(d)).[54] The other peaks at 461 and 455.4 eV are attributed to Ti $2p_{1/2}$ and Ti $2p_{3/2}$ originating from Ti–O bonding.[54] As reported previously, the Ti–O bond develops in MXene–GO hydrogels/aerogels due to the surface oxidation of MXene with the functional groups of GO layers.[55] Nonetheless, as no discernible TiO_2 peaks were observed in the XRD pattern, the oxidation process may not be significantly pronounced. In addition, the XPS spectrum of C 1s is fitted into four core energy levels with binding energies of 284.5, 285, 287.5, and 291.9 eV for C–C, C–O, C═O, and C–F_2, respectively (Fig. 6(e)).[56] The deconvoluted O 1s XPS spectrum shows peaks at 529.8/530.9, 532.1 and 534.3 eV related to Ti–O, Ti–OH and H_2O, respectively.[35]

3.5. TGA analysis

The thermal decomposition behavior of NiVSe, NiVSe-GAF, and NiVSe–MXene-GAF was studied through TGA analysis under air atmosphere and the results are presented in Fig. 7(a). The pristine NiVSe exhibits an initial weight loss up to 300 °C, primarily attributed to the release of entrapped water molecules and volatile components. Subsequently, the transformation of NiVSe to the corresponding oxides results in rise of TGA curve within the temperature range of 300–450 °C.[57] After that the sublimation of SeO_2 causes a substantial decrease in the weight of NiVSe, culminating in a total loss of 41.3% by 700 °C. NiVSe-GAF and NiVSe–MXene-GAF also show an inconspicuous rise in the TGA curve with a small shift in the inflection point of major weight loss from 450 to 430 °C as compared to NiVSe. For NiVSe-GAF and NiVSe–MXene-GAF, the initial weight changes after the removal of entrapped water include the removal of surface functionalities of MXene and rGO, and thermal transformation of NiVSe to oxides, accompanied by the oxidation of MXene to TiO_2 in the latter aerogel foam.[58] The subsequent major weight loss for the aerogel foam is due to the rapid burning of carbon content of NiVSe-GAF and NiVSe–MXene-GAF leading to total weight loss of 78.4% and 70.1%, respectively. Furthermore, as indicated by the TGA curves, the impregnation of MXene provides thermal stability to NiVSe–MXene-GAF compared to NiVSe-GAF which is in accordance with the previous reports on MXene composites.[59]

3.6. *I–V* measurements

To evaluate the impact of impregnation of NiVSe into aerogel foams on the electrical conductivity of resultant materials, *I–V* measurements were conducted. For this purpose, NiVSe, NiVSe-GAF, and NiVSe–MXene-GAF were transformed into pellets using a hydraulic press. As depicted in Fig. 7(b), all prepared materials, including the pristine NiVSe, demonstrate proficient adherence to Ohm's law within a voltage range of 0.4 to −0.4 V, showcasing fairly straight *I–V* curves along the current–voltage axis owing to the impressive conductive properties of metal selenides. However, aerogel foam composites exhibited a greater response to voltage changes, indicating low intrinsic resistance, with NiVSe–MXene-GAF being the most

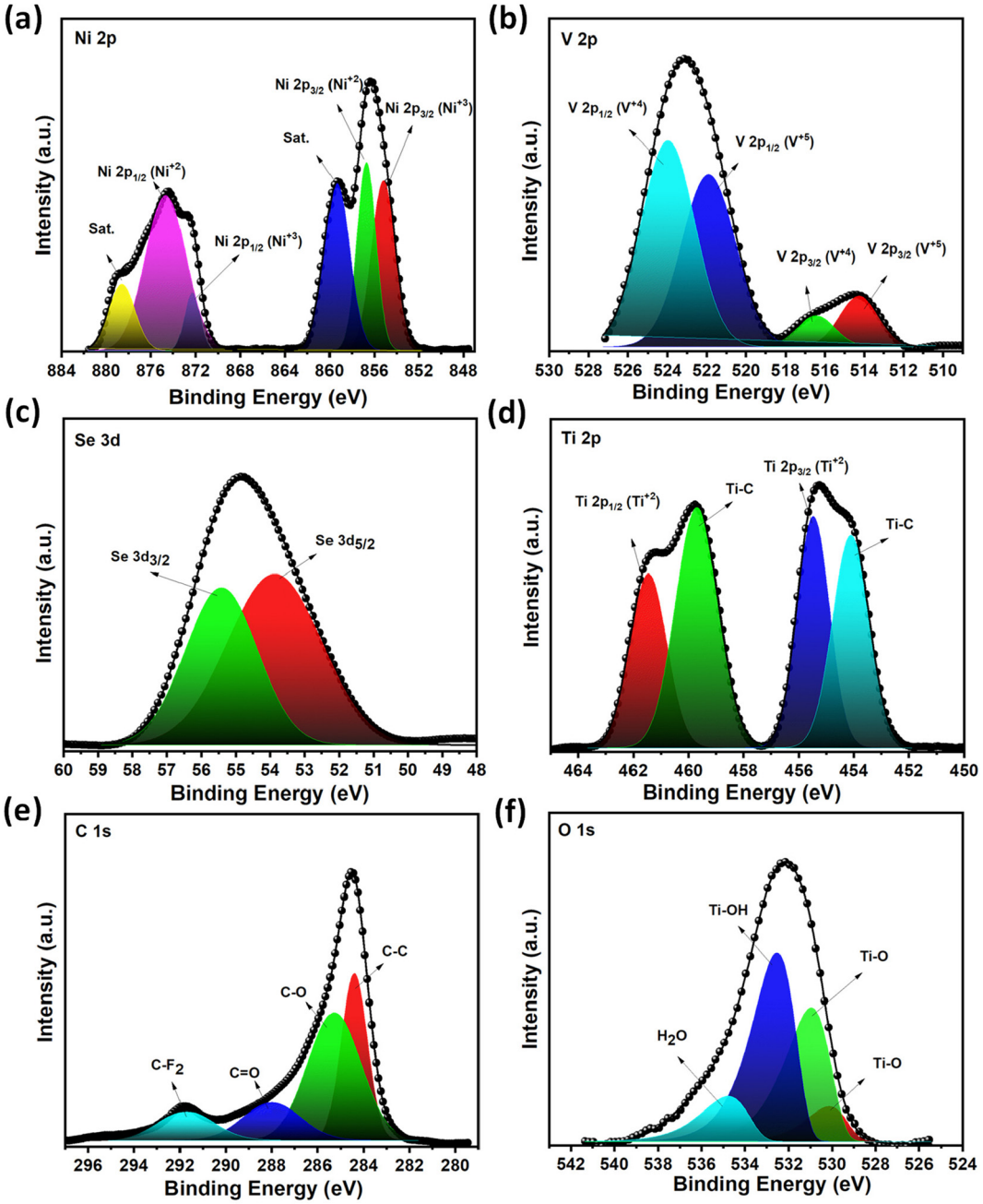

Fig. 6 XPS analysis of NiVSe–MXene-GAF; high-resolution deconvoluted spectra of (a) Ni 2p, (b) V 2p, (c) Se 3d, (d) Ti 2p, (e) C 1s, and (f) O 1s.

active to voltage changes. The electrical conductivity (σ) for each material was calculated using eqn (1):[36]

$$\sigma = \frac{w}{R \times A} \quad (1)$$

in the above equation, w, R, and A denote the width, resistance, and area of the pellet, respectively. The calculated values of electrical conductivity for NiVSe, MXene, NiVSe-GAF, and NiVSe–MXene-GAF were found as 14.1, 70.5, 33.3, and 51.7 S m^{-1}, respectively. The highest electrical conductivity observed for NiVSe–MXene-GAF after pure MXene is attributed to the synergism and generation of ohmic contacts among the individual components *i.e.*, NiVSe, MXene, and rGO. This enhanced electrical conductivity of NiVSe–MXene-GAF will facilitate the rapid transport of electrons during the redox reactions. In addition, the low internal resistance will minimize the voltage fluctuations during charge–discharge, preventing undesirable side reactions and degradation of active material during the electrochemical process.

3.7. BET analysis

N_2 adsorption–desorption experiments were carried out at 77 K to determine the specific surface area and porous charac-

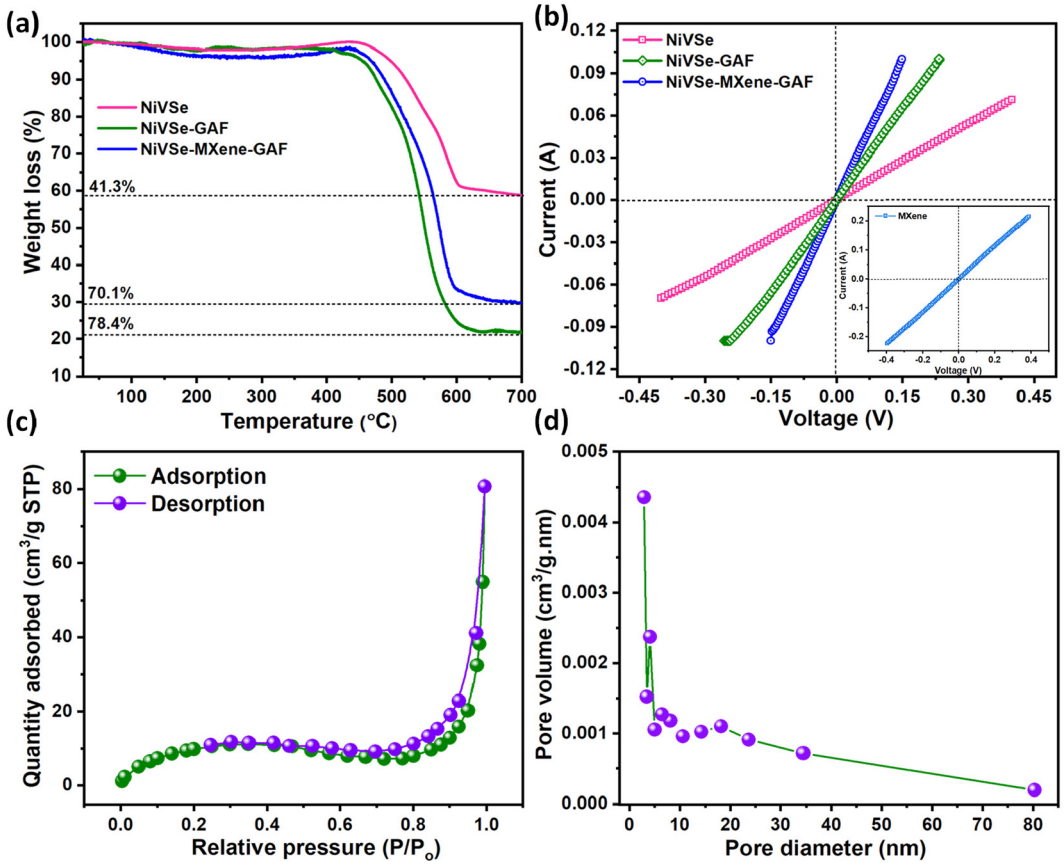

Fig. 7 (a) TGA curves of NiVSe, NiVSe-GAF, and NiVSe–MXene-GAF, (b) *I*–*V* plots of NiVSe, NiVSe-GAF, and NiVSe–MXene-GAF; inset shows the *I*–*V* plot for pure MXene, (c) N_2 adsorption–desorption isotherms for NiVSe–MXene-GAF, and (d) the BJH desorption pore size distribution plot for NiVSe–MXene-GAF.

teristics of NiVSe–MXene-GAF. The N_2 adsorption–desorption plot in Fig. 7(c) resembles type-IV isotherm with a vague knee at low pressure due to the monolayer adsorption, followed by multi-layer adsorption. The isotherm shows a typical H3 hysteresis loop at intermediate pressures, indicating the existence of mesopores in the aerogel foam. The absence of a saturation point at P/P_0 = 1 suggests a wide distribution of pore sizes.

The BJH desorption pore size distribution curve in Fig. 7(d) exhibits double peak pore diameters at 4.1 nm and 18.1 nm, within an overall pore size distribution range of 2.8–80 nm. The BET specific surface area calculated from the N_2 adsorption–desorption isotherm was found to be 37.8 $m^2\ g^{-1}$. The BJH desorption pore diameter and pore volume were calculated to be 24.2 nm and 0.124 $cm^3\ g^{-1}$.

3.8. Supercapacitor measurements

Supercapacitor performance analysis was carried out using CV, GCD, and EIS measurements in 3 M KOH solution at room temperature. Fig. 8(a) shows the comparative CV plots of the Ni foam substrate, NiVSe, NiVSe-GAF, and NiVSe–MXene-GAF electrodes with an operative potential window of 0 to 0.5 V at a constant scan rate of 100 mV s^{-1}. Ni foam as the substrate material showed quite a weak CV signal, inferring the insignificant contribution to the current density achieved by the active materials. For the electrodes under analysis, the CV signal was in the following order: NiVSe–MXene-GAF > NiVSe-GAF > NiVSe, which apparently indicates improvement in the charge storing capacity for NiVSe integrated aerogel foams. Among them, NiVSe–MXene-GAF delivered the largest CV area and redox peak intensity, suggesting excellent redox kinetics and charge storage resulting from improved active centers for redox reactions and adsorption of ions. In all cases, a redox couple is ascribed to the redox characteristics of Ni ($Ni^{2+} \leftrightarrow Ni^{3+}$) and V ($V^{4+} \leftrightarrow V^{5+}$) in accordance with the previous reports.[39] Scan rate-dependent CV plots for NiVSe, NiVSe-GAF, and NiVSe–MXene-GAF are presented in Fig. 8(b–d), ranging from 5 to 100 mV s^{-1}. As depicted, the progression of the scan rate is accompanied by the increase in the current density and a small shift of the maxima of redox couple towards anodic and cathodic extremes. This peak shift with an increase in the scan rate is due to the polarization behavior of the active material.[60] Nonetheless, the shape of CV curves remained well-maintained at all scan rates demonstrating the capability of electrodes to deliver high-rate performance that will be further discussed in the later section.

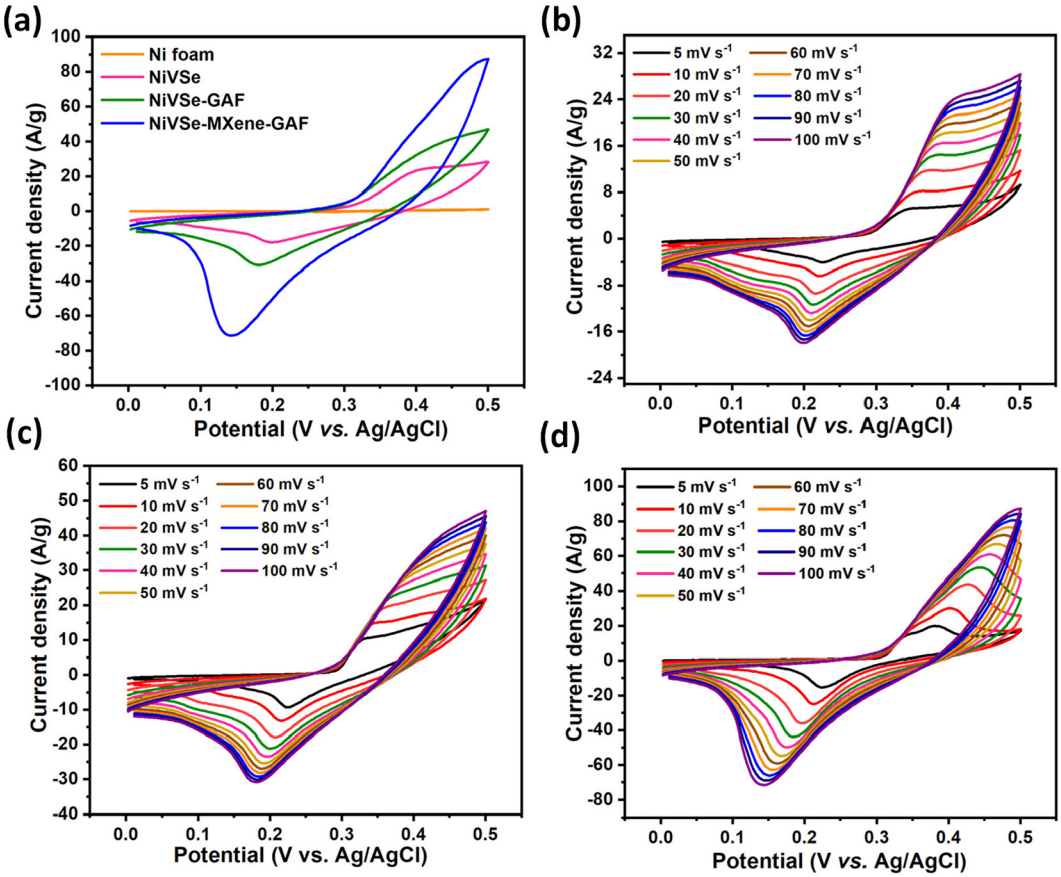

Fig. 8 (a) CV plots of Ni foam, NiVSe, NiVSe-GAF, and NiVSe–MXene-GAF at a scan rate of 100 mV s^{-1}; CV plots of (b) NiVSe (c) NiVSe-GAF, and (d) NiVSe–MXene-GAF at various scan rates (5–100 mV s^{-1}).

The GCD plots of NiVSe, NiVSe-GAF, and NiVSe–MXene-GAF at a constant current density of 1 A g^{-1} are displayed in Fig. 9(a). A potential dependent plateau along the charge-discharge curves originates from the battery-type charge storage characteristics of NiVSe.[61] As expected, NiVSe–MXene-GAF exhibits the largest discharge time (~1108 s) greater than NiVSe-GAF (~899 s) and NiVSe (~520 s) at 1 A g^{-1}, reaffirming the superior electrochemical performance of NiVSe–MXene-GAF among all electrodes. In addition, the GCD for NiVSe–MXene-GAF showed a smaller *IR* drop as compared to NiVSe-GAF and NiVSe signifying relatively smaller equivalent series resistance (ESR). The initial coulombic efficiency (ICE) for NiVSe, NiVSe-GAF, and NiVSe–MXene-GAF was calculated to be 91.4%, 95.9%, and 99.2%, respectively. Generally, the ICE value of energy storing material is greatly affected by its internal resistance. This internal resistance consumes some of the energy during the discharge period and therefore the discharge energy is always less than the energy stored in the material. Additionally, the intense electrochemical reactions also lead to a further increase in the internal resistance. Hence, the high ICE value for NiVSe–MXene-GAF as compared to NiVSe and NiVSe-GAF correlates with its small internal resistance and authenticates a uniform charge–discharge process.[62] Furthermore, similar to the CV results, GCD plots are symmetric in nature irrespective of the applied current density, reflecting good reversibility of the electrochemical processes occurring at the electrode–electrolyte interface (Fig. 9(b–d)). The mass-specific energy storage capacity of each electrode was determined from GCD data at different current densities (1–12 A g^{-1}) using the following eqn (2):[63]

$$\text{Specific capacity (mA h g}^{-1}) = \frac{I \times \Delta t}{m \times 3.6} \quad (2)$$

where I is the current density, Δt denotes the discharge time, and m is the mass of the active material. The maximum specific capacity for NiVSe–MXene-GAF was observed at 1 A g^{-1} as 305.8 mA h g^{-1}. This value is almost 2.21- and 1.35-fold of the specific capacity calculated for NiVSe (138.3 mA h g^{-1}) and NiVSe-GAF (226.3 mA h g^{-1}). The results infer that the incorporation of NiVSe in an aerogel form not only improved the charge storing capacity of the electrode but MXene functionalized aerogel foam evidently underpins better intrinsic characteristics than NiVSe-GAF, which results in the substantially effective utilization of NiVSe. Other than the specific capacity at 1 A g^{-1}, NiVSe–MXene-GAF sustained a higher value of specific capacity at

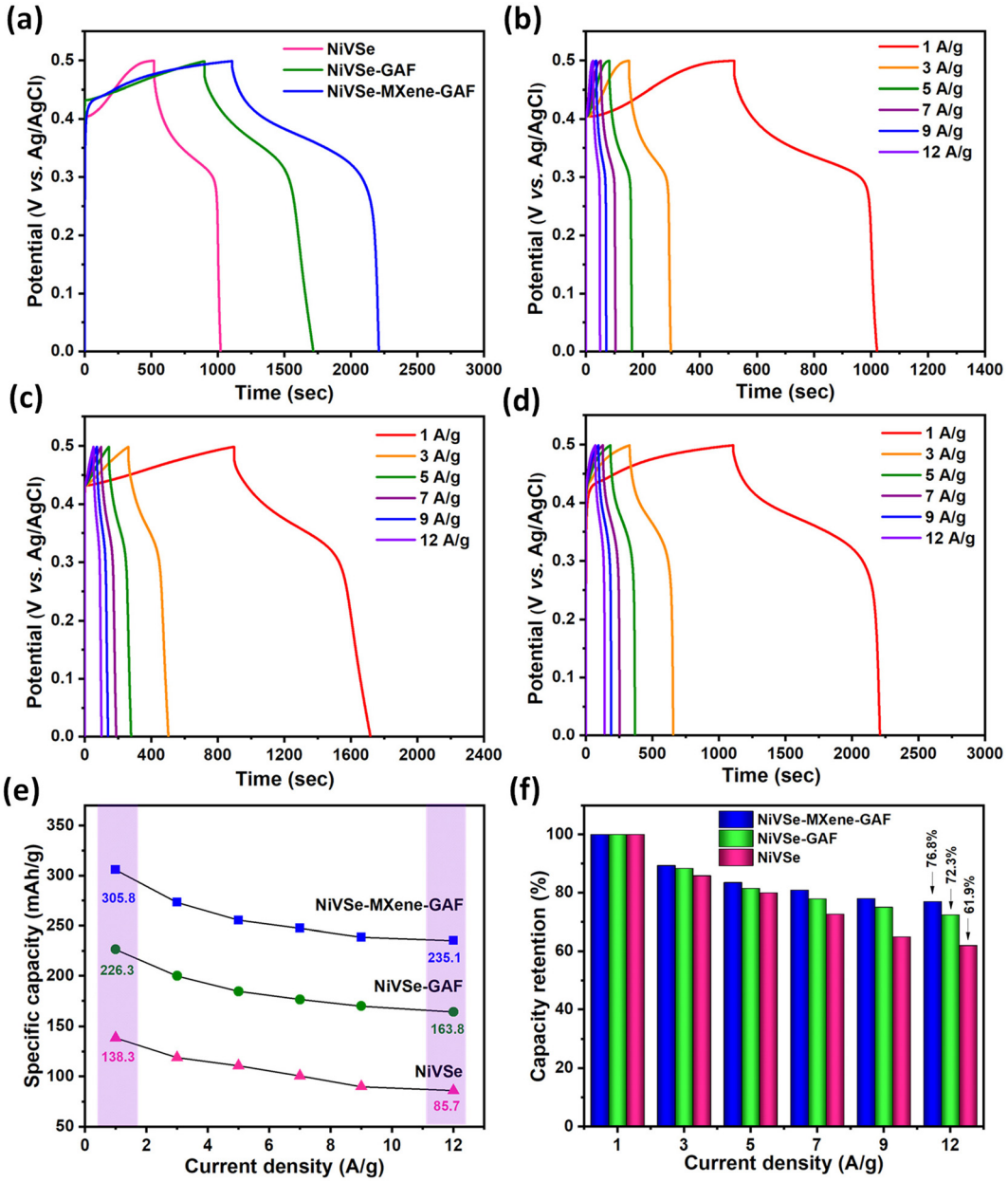

Fig. 9 (a) GCD plots of NiVSe, NiVSe-GAF, and NiVSe–MXene-GAF at a current density of 1 A g^{-1}; GCD plots of (b) NiVSe, (c) NiVSe-GAF, and (d) NiVSe–MXene-GAF at various current densities (1–12 A g^{-1}), (e) trend in specific capacity *vs.* current density for NiVSe, NiVSe-GAF, and NiVSe–MXene-GAF, and (f) capacity retention of NiVSe, NiVSe-GAF, and NiVSe–MXene-GAF with an increase in the current density.

all current densities as compared to its analogs (Table S1† and Fig. 9(e)). The percentage retention or rate performance of NiVSe, NiVSe-GAF, and NiVSe–MXene-GAF is shown in Fig. 9(f). As a general phenomenon, with the progressive current density a decline in the charge storage capacity was observed for all electrodes because of limited time for electrolyte ions to diffuse into active material to take part in the charge storage process.[64] Besides, on comparison, NiVSe–MXene-GAF exhibited the highest capacity retention of 76.8% even at a very high current density of 12 A g^{-1} as compared to NiVSe (61.9%) and NiVSe-GAF (72.3%).

To analyze the mechanism of charge storage in NiVSe–MXene-GAF, the diffusion and capacitive role was investigated by applying the following power law eqn (3):[65]

$$\log i(\nu) = \log a + b \log \nu \quad (3)$$

where i is the anodic or cathodic peak current density at the scan rate of ν; a and b are the fitting parameters in the equation. Assuming a linear fit, the value of b was determined from the log–log plot in Fig. 10(a). It has been theorized that the value of slope b = 0.5 and 1 accounts for the diffusional

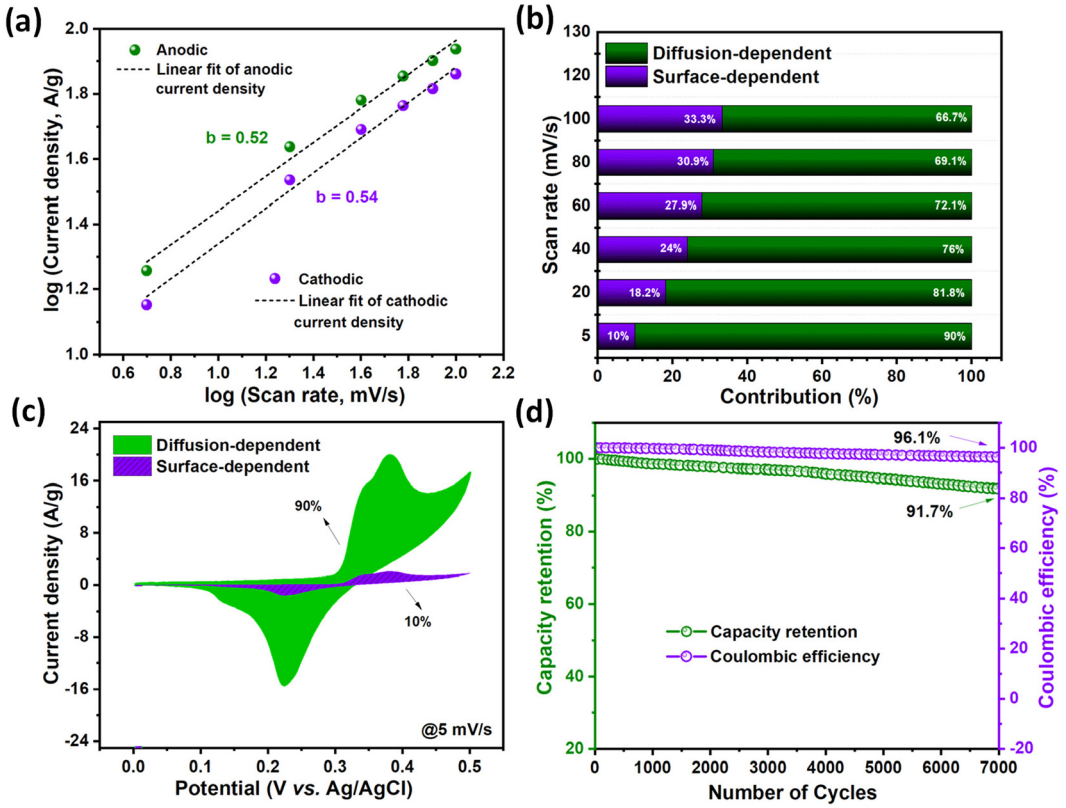

Fig. 10 (a) Power law plot for NiVSe–MXene-GAF, (b) percentage of diffusion and surface distribution at various scan rates (5–100 mV s^{-1}), (c) deconvoluted current density for diffusion and surface contribution at 5 mV s^{-1}, (d) cycling performance of NiVSe–MXene-GAF for 7000 GCD cycles.

and capacitive mechanism of charge storage. For NiVSe–MXene-GAF, the anodic and cathodic current density presented in Fig. 10(a) fall within the range of 0.52 and 0.54, respectively indicating a hybrid behavior of the electrode. The current response at each scan rate was further divided to diffusion dependent and surface dependent capacitive contributions using the Dunn's relation in the following eqn (4):[66]

$$i(V) = k_1\nu + k_2\nu^{1/2}. \quad (4)$$

According to the above equation, the current density at any fixed voltage V involves a combined contribution from the diffusion-controlled ($k_1\nu$) and surface-dependent capacitive processes ($k_2\nu$). Capacitive contribution from NiVSe–MXene-GAF at a very small scan rate (10% at 5 mV s^{-1}) is significant and certainly contributed by the carbon content of the aerogel foam due to the formation of an electrical double layer (EDL). Nonetheless, the deconvoluted current density in Fig. 10(b and c) at various scan rates (5–100 mV s^{-1}) shows major contribution from diffusion-dependent processes even at high scan

Table 1 Comparison of the supercapacitor performance of NiVSe–MXene-GAF with those of already reported similar electrode materials

Material	Specific capacitance	Cycling stability	Ref.
NiVSe–MXene-GAF	305.8 mA h g^{-1} at 1 A g^{-1}	91.7%@7000 cycles	This work
Ni(Co)Se_2@Co(Ni)Se_2	264.5 mA h g^{-1} at 1 A g^{-1}	—	67
VSe_2/rGO	156.8 mA h g^{-1} at 1 A g^{-1}	89.76%@7000 cycles	68
rGO/MXene@NiCo–P	214.66 mA h g^{-1} at 1 A g^{-1}	70.87%@10 000 cycles	69
Graphene-coated MXene Ni–Mn LDH	241.9 mA h g^{-1} at 1 A g^{-1}	94.7%@4000 cycles	70
P–Ti_3C_2@$NiCo_2S_4$	135 mA h g^{-1} at 1 A g^{-1}	—	71
$Ni_3V_2O_8$@Co–B	216.1 mA h g^{-1} at 1 A g^{-1}	—	72
Ti_3C_2/$Ni_2CO_3(OH)_2$	173.8 mA h g^{-1} at 1 A g^{-1}	72.5%@5000 cycles	74
Ni$(OH)_2$/graphene	238 mA h g^{-1} at 0.8 A g^{-1}	91.6%@2000 cycles	75
VS_4/rGO/CoS_2@Co	274.3 mA h g^{-1} at 0.6 A g^{-1}	89.6%@20 000 cycles	76
CNT@Ni$(OH)_2$	167 mA h g^{-1} at 2 A g^{-1}	92%@1000 cycles	77
Ni_2Co-LDHs@Al–Ti_3C_2 MXene	227 mA h g^{-1} at 1 A g^{-1}	90%@10 000 cycles	78
(Ni,Co)Se_2@Nb_2CT_x	267.1 mA h g^{-1} at 1 A g^{-1}	96.8%@10 000 cycles	73

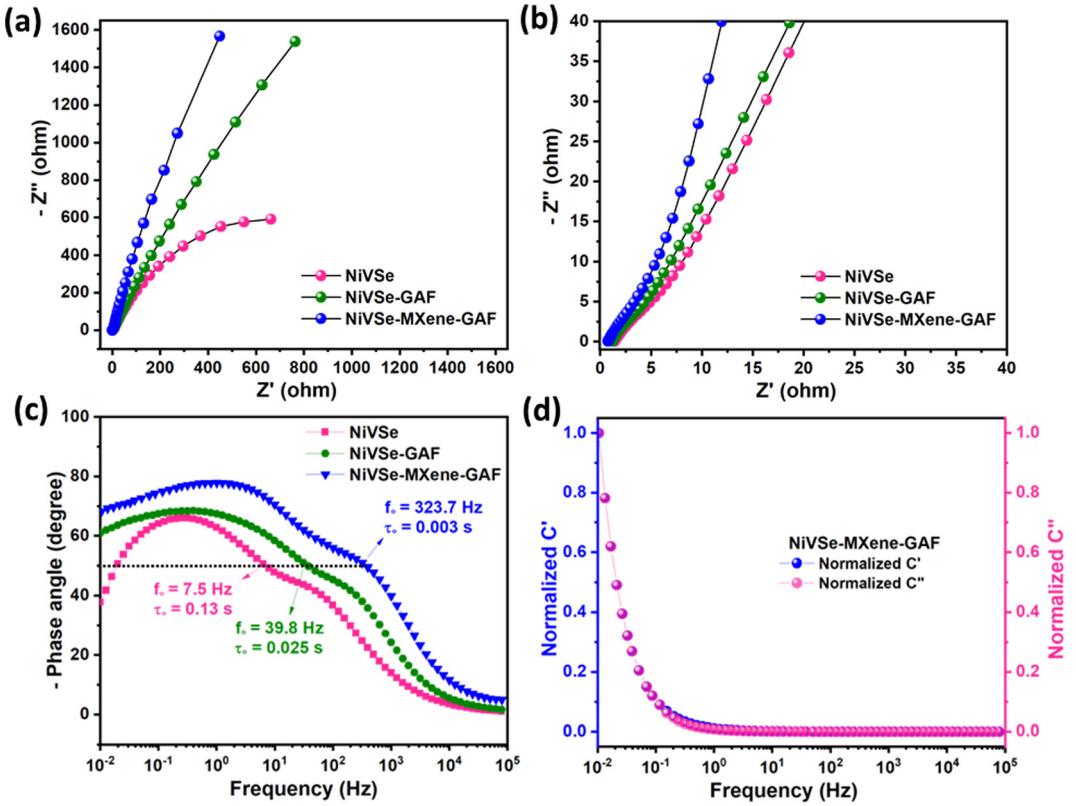

Fig. 11 EIS measurements: (a) Nyquist plots for NiVSe, NiVSe-GAF, and NiVSe–MXene-GAF, (b) magnified high-frequency region of Nyquist plots (c) Bode plots for NiVSe, NiVSe-GAF, and NiVSe–MXene-GAF, and (d) normalized real (*C*′) and imaginary (*C*″) capacitance *vs.* applied frequency.

rates where mostly the surface of the electrode contributes to charge storage. This appreciable retention of diffusional processes is speculated to be due to the improved transport of electrolyte ions originating from multi-dimensional open porous channels and shortening of the ion-diffusion path in NiVSe–MXene-GAF. This pores-rich 3D structure and high conductivity of MXene-GAF backbone also played a significant role in considerable capacity retention of NiVSe–MXene-GAF at high current densities (Fig. 9(f)).

Cycling stability is the most significant parameter in the study of an energy storage system. The cycling stability of NiVSe–MXene-GAF was evaluated for consecutive 7000 GCD cycles at a constant current density of 12 A g^{-1} (Fig. 10(d)). NiVSe–MXene-GAF retained 91.7% of its initial capacity with 96.1% retention of coulombic efficiency after 7000 cycles. This outstanding cycling efficiency indicates the chemical and mechanical stability of the NiVSe–MXene-GAF heterostructure. Henceforth, the integration of NiVSe in MXene-GAF not only prevents the active material from aggregation but the porous 3D skeleton of aerogel foam buffers out the volume changes during the continuous charge–discharge cycles. Table 1 provides a comparison of the specific capacity and cycling stability of NiVSe–MXene-GAF with already reported similar electrode materials such as Ni(Co)Se_2@Co(Ni)Se_2,[67] VSe_2/rGO,[68] rGO/MXene@NiCo–P,[69] graphene-coated MXene Ni–Mn LDH,[70] P–Ti_3C_2@$NiCo_2S_4$,[71] $Ni_3V_2O_8$@Co–B,[72] and (Ni,Co)Se_2@Nb_2CT_x.[73]

The supercapacitor performance of NiVSe–MXene-GAF was found to be comparable to or even greater than most electrode materials.

To investigate the impedance behavior and dynamics of the electrochemical process EIS studies were performed within the frequency range of 0.01 to 100 kHz. The Nyquist plots derived

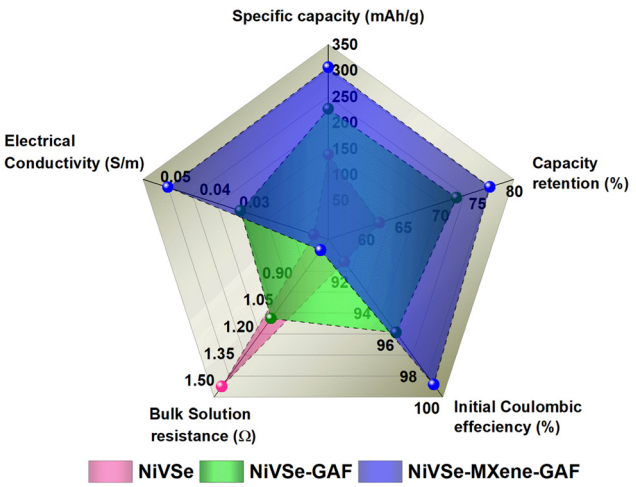

Fig. 12 Radar plot showing comparison of different performance characteristics of NiVSe, NiVSe-GAF, and NiVSe–MXene-GAF.

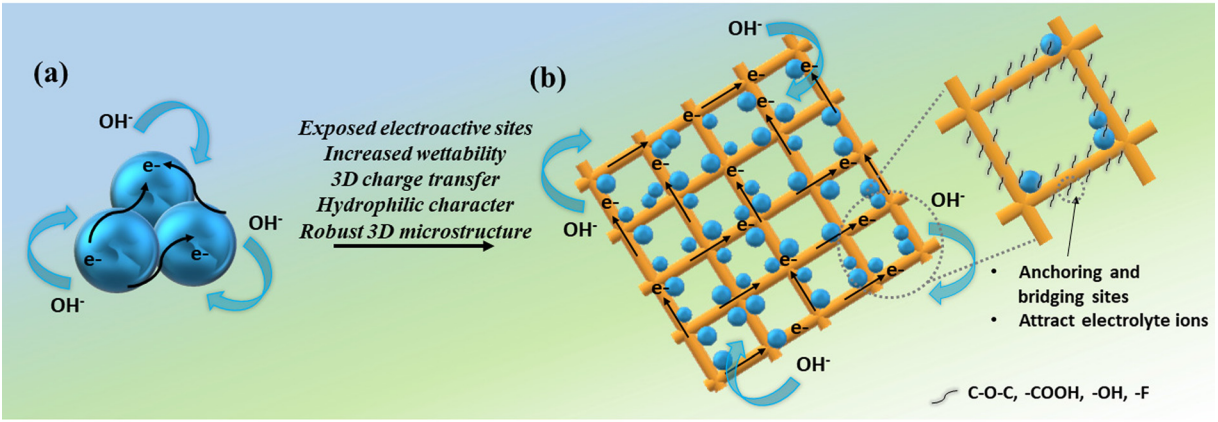

Fig. 13 Schematic diagram showing the effect of NiVSe integration into MXene-GAF for enhanced supercapacitor performance; (a) NiVSe and (b) NiVSe-MXene-GAF.

from the EIS data are presented in Fig. 11(a and b). The *x*-intercept of Nyquist represents bulk solution resistance (R_s) which embraces the intrinsic resistance of the active material, electrolyte resistance, and contact resistance at the active material and electrolyte interface.[79] The magnified high frequency region of Nyquist in Fig. 11(b) displays the lowest R_s value for NiVSe–MXene-GAF (0.71 Ω) preceded by NiVSe-GAF (1.09 Ω) and NiVSe (1.47 Ω). The straight line of Nyquist persuading towards the low frequency region indicates the Warburg resistance (R_w) for the diffusion of ions. A steeper slope of the Warburg line for NiVSe–MXene-GAF as compared to NiVSe-GAF and NiVSe interprets that with the incorporation of NiVSe within the MXene-GAF, the resistance to ion diffusion remarkably decreased leading to an increase in both the specific capacity and rate capability. Additionally, the Warburg line is inclined at approximately 45° for NiVSe, and the angle increases as we proceed to NiVSe-GAF and NiVSe–MXene-GAF which is attributed to the capacitive behavior of carbon contents of aerogel foams. The obtained results from the Nyquist plots corroborate well with the CV and GCD findings.

For further understanding, Bode phase angle plots are shown in Fig. 11(c) which display changes in the phase angle with the applied frequency. The phase angle for a supercapacitor fluctuates among two extremes *i.e.*, 0° for a resistor and 90° for an ideal capacitor. The phase angles at tail for NiVSe, NiVSe-GAF, and NiVSe–MXene-GAF are 37.5°, 60.7° and 67.4° referring to improved capacitor characteristics for NiVSe–MXene-GAF.[80] The relaxation time ($\tau_0 = 1/f_0$) at knee frequency (f_0) is related to the time required to discharge the stored energy at the electrode with an efficiency more than of 50%. As depicted in Fig. 11(c), a small relaxation time for NiVSe–MXene-GAF (0.003 s) than NiVSe-GAF (0.025 s) and NiVSe (0.13 s) indicates fast charge–discharge kinetics. The variation in real (C') and imaginary (C'') components of the capacitance with the frequency is represented in Fig. 11(d) for NiVSe–MXene-GAF. As can be seen, the capacitance is high at low frequency and approaches null at the highest frequency where the electrode acts like a resistor.[81]

The radar plot in Fig. 12 provides a comparison of different performance parameters of NiVSe, NiVSe-GAF, and NiVSe–MXene-GAF which evidently represent that the integration of NiVSe into MXene-GAF significantly improved the overall electrochemical performance of NiVSe–MXene-GAF. This enhanced electrochemical performance can be accredited to (i) the increased electroactive surface area due to the open and porous structure of aerogel foam, and combined contribution from NiVSe (*i.e.*, battery-type redox reactions) and MXene-GAF (*i.e.*, EDL) towards charge storage, (ii) increased wettability or easy access of electrolyte ions from multiple dimensions to active sites, endowed by 3D porous channels (iii) surface functionalities that subsidize the hydrophilic character to MXene-GAF for electrolyte ion attraction and act as anchoring sites for NiVSe particles to bridge conductive channels among NiVSe and MXene-GAF, (iv) large surface area and 3D charge transfer over the highly conductive MXene-GAF, and (v) flexible and robust 3D framework of NiVSe–MXene-GAF (Fig. 13).

4. Conclusions

In summary, bimetallic NiVSe was incorporated into 3D hierarchical MXene-GAF to improve the electroactive surface area and electrical conductivity and impede the degradation of the battery-type material during the electrochemical process. 3D porous pathways, improved conductive properties, enriched active sites of NiVSe, and the heterostructure interface of NiVSe–MXene-GAF enhanced the supercapacitor performance of the prepared electrode as compared to its analogs NiVSe and NiVSe-GAF. NiVSe–MXene-GAF delivered a high specific capacity of 305.8 mA h g^{-1} at 1 A g^{-1}, greater than those of NiVSe (138.3 mA h g^{-1}) and NiVSe-GAF (226.3 mA h g^{-1}). In addition, NiVSe–MXene-GAF exhibited a high rate performance (235.1 mA h g^{-1} at 12 A g^{-1}), excellent cycling stability with 91.7% retention of specific capacity and 96.1% coulombic efficiency after 7000 GCD cycles. Impedance measurements showed a reduction in solution resistance for NiVSe–MXene-

GAF (R_s = 0.71 Ω) compared to those of NiVSe-GAF (R_s = 1.09 Ω) and NiVSe (R_s = 1.47 Ω). Hence, this work paves the way for the development of high-performance 3D multicomponent microstructures for efficient supercapacitor devices. Based on the outstanding results, we plan to evaluate the efficiency of NiVSe–MXene-GAF in a two-electrode configuration and construct a supercapacitor device.

Data availability

All data generated or analyzed during this study are included in the main article and the ESI.†

Conflicts of interest

The authors have no conflicts of interest to declare.

Acknowledgements

The authors extend their appreciation to Taif University, Saudi Arabia, for supporting this work through the project number (TU-DSPP-2024-28). Prof. Dr Sonia Zulfiqar is highly thankful for the support provided by the Statutory City of Ostrava, Czechia, through Research Grant "Global Experts". Prof. Cochran and Prof. Zulfiqar are grateful for the XPS measurements provided by Dr Dapeng Jing of the Materials Analysis and Research Laboratory of the Iowa State University Office of Biotechnology. E. W. C. and S. Z. are also thankful to the National Science Foundation for financial support through research grants NSF-2113695, NSF-2218070 and NSF-2242763. The authors are also thankful to the Institute of Chemistry, Baghdad-ul-Jadeed Campus, The Islamia University of Bahawalpur, Pakistan.

References

1 D. P. Chatterjee and A. K. Nandi, A review on the recent advances in hybrid supercapacitors, *J. Mater. Chem. A*, 2021, **9**, 15880–15918.
2 P. Naskar, A. Maiti, P. Chakraborty, D. Kundu, B. Biswas and A. Banerjee, Chemical supercapacitors: a review focusing on metallic compounds and conducting polymers, *J. Mater. Chem. A*, 2021, **9**, 1970–2017.
3 M. Usman, S. Nisar, D.-k. Kim, S. Golovynskyi, M. Imran, G. Dastgeer and L. Wang, Polarization-sensitive photodetection of anisotropic 2D black arsenic, *J. Phys. Chem. C*, 2023, **127**, 9076–9082.
4 K. Gong, H. Lee, Y. Choi, G. Jung, K. Keum, J. W. Kim and J. S. Ha, A flexible supercapacitor with high energy density and wide range of temperature tolerance using a high-concentration aqueous gel electrolyte, *Electrochim. Acta*, 2024, **475**, 143585.
5 G. Dastgeer, S. Nisar, A. Rasheed, K. Akbar, V. D. Chavan, D.-k. Kim, S. M. Wabaidur, M. W. Zulfiqar and J. Eom, Atomically engineered, high-speed non-volatile flash memory device exhibiting multibit data storage operations, *Nano Energy*, 2024, **119**, 109106.
6 A. Patra, K. Namsheer, J. R. Jose, S. Sahoo, B. Chakraborty and C. S. Rout, Understanding the charge storage mechanism of supercapacitors: in situ/operando spectroscopic approaches and theoretical investigations, *J. Mater. Chem. A*, 2021, **9**, 25852–25891.
7 F. Xing, Z. Bi, F. Su, F. Liu and Z. S. Wu, Unraveling the design principles of battery–supercapacitor hybrid devices: from fundamental mechanisms to microstructure engineering and challenging perspectives, *Adv. Energy Mater.*, 2022, **12**, 2200594.
8 X. Yun, T. Lu, R. Zhou, Z. Lu, J. Li and Y. Zhu, Heterostructured $NiSe_2/CoSe_2$ hollow microspheres as battery-type cathode for hybrid supercapacitors: Electrochemical kinetics and energy storage mechanism, *Chem. Eng. J.*, 2021, **426**, 131328.
9 G. Dastgeer, A. M. Afzal, G. Nazir and N. Sarwar, p-GeSe/n-ReS_2 heterojunction rectifier exhibiting a fast photoresponse with ultra-high frequency-switching applications, *Adv. Mater. Interfaces*, 2021, **8**, 2100705.
10 S. Nisar, M. Shahzadi, Z. M. Shahzad, D.-k. Kim, G. Dastgeer and A. Irfan, $MoTe_2$ field-effect transistor for the rapid detection of streptavidin via engineered support construct, *ACS Appl. Electron. Mater.*, 2023, **5**, 5714–5721.
11 B. Kirubasankar, V. Murugadoss, J. Lin, T. Ding, M. Dong, H. Liu, J. Zhang, T. Li, N. Wang and Z. Guo, In situ grown nickel selenide on graphene nanohybrid electrodes for high energy density asymmetric supercapacitors, *Nanoscale*, 2018, **10**, 20414–20425.
12 B. Pandit, S. R. Rondiya, S. Shegokar, L. K. Bommineedi, R. W. Cross, N. Y. Dzade and B. R. Sankapal, Combined electrochemical and DFT investigations of iron selenide: a mechanically bendable solid-state symmetric supercapacitor, *Sustainable Energy Fuels*, 2021, **5**, 5001–5012.
13 H. Peng, G. Ma, K. Sun, Z. Zhang, J. Li, X. Zhou and Z. Lei, A novel aqueous asymmetric supercapacitor based on petal-like cobalt selenide nanosheets and nitrogen-doped porous carbon networks electrodes, *J. Power Sources*, 2015, **297**, 351–358.
14 L. Fan, Z. Feng, X. Zhu, Y. Wei, Q. Zhang, Y. Cao and L. Zhu, Synthesis of nanosphere-like vanadium selenide cathode for high performance asymmetric hybrid supercapacitors, *Electrochim. Acta*, 2023, **465**, 142970.
15 S. Xie, J. Gou, B. Liu and C. Liu, Nickel-cobalt selenide as high-performance and long-life electrode material for supercapacitor, *J. Colloid Interface Sci.*, 2019, **540**, 306–314.
16 S. E. Moosavifard, F. Saleki, A. Mohammadi, A. Hafizi and M. R. Rahimpour, Construction of hierarchical nanoporous bimetallic copper–cobalt selenide hollow spheres for hybrid supercapacitor, *J. Electroanal. Chem.*, 2020, **871**, 114295.

17 Y.-L. Liu, C. Yan, G.-G. Wang, F. Li, Q. Kang, H.-Y. Zhang and J.-C. Han, Selenium-rich nickel cobalt bimetallic selenides with core–shell architecture enable superior hybrid energy storage devices, *Nanoscale*, 2020, **12**, 4040–4050.
18 H. Liu, X. Liu, S. Wang, H.-K. Liu and L. Li, Transition metal based battery-type electrodes in hybrid supercapacitors: A review, *Energy Storage Mater.*, 2020, **28**, 122–145.
19 G. Dastgeer, S. Nisar, Z. M. Shahzad, A. Rasheed, D. k. Kim, S. H. A. Jaffery, L. Wang, M. Usman and J. Eom, Low-Power Negative-Differential-Resistance Device for Sensing the Selective Protein via Supporter Molecule Engineering, *Adv. Sci.*, 2023, **10**, 2204779.
20 D. Khalafallah, M. Zhi and Z. Hong, Rational engineering of hierarchical mesoporous Cu_xFe_ySe battery-type electrodes for asymmetric hybrid supercapacitors, *Ceram. Int.*, 2021, **47**, 29081–29090.
21 M. G. Park, J. W. Choi, I. W. Ock, G. H. Kim and J. K. Kang, Mesoporous Thorn-Covered Core–Shell Cathode and 3D Reduced Graphene Oxide Aerogel Composite Anode with Conductive Multivalence Metal Sulfides for High-Performance Aqueous Hybrid Capacitors, *Adv. Energy Mater.*, 2021, **11**, 2003563.
22 H. Zhou, Y. Zhan, F. Guo, S. Du, B. Tian, Y. Dong and L. Qian, Synthesis of biomass-derived carbon aerogel/MnO_x composite as electrode material for high-performance supercapacitors, *Electrochim. Acta*, 2021, **390**, 138817.
23 M. Yu, Y. Han, J. Li and L. Wang, One-step synthesis of sodium carboxymethyl cellulose-derived carbon aerogel/nickel oxide composites for energy storage, *Chem. Eng. J.*, 2017, **324**, 287–295.
24 H. Gholipour-Ranjbar, M. R. Ganjali, P. Norouzi and H. R. Naderi, Synthesis of cross-linked graphene aerogel/Fe_2O_3 nanocomposite with enhanced supercapacitive performance, *Ceram. Int.*, 2016, **42**, 12097–12104.
25 S. A. Mirkhani, A. Shayesteh Zeraati, E. Aliabadian, M. Naguib and U. Sundararaj, High dielectric constant and low dielectric loss via poly (vinyl alcohol)/$Ti_3C_2T_x$ MXene nanocomposites, *ACS Appl. Mater. Interfaces*, 2019, **11**, 18599–18608.
26 H. H. Udhayakumar, Y. H. Park, E. Park, G. Murali, S. Park, J. Kim, J. Yeon, S. J. Lee, S. Kim and H. Yang, Highly oxidation resistant and organic dispersible ligand functionalized MXene for triggering performance of lithium ion batteries, *Chem. Eng. J.*, 2024, **488**, 150699.
27 S. R. KA, N. Barman, K. Namsheer, R. Thapa and C. S. Rout, $CrSe_2$/Ti_3C_2 MXene 2D/2D hybrids as promising candidates for energy storage applications, *Sustainable Energy Fuels*, 2022, **6**, 5187–5198.
28 S. Zhao, W. Ran, L. Wang and G. Shen, Interlocked MXene/rGO aerogel with excellent mechanical stability for a health-monitoring device, *J. Semicond.*, 2022, **43**, 082601.
29 R. Nirlakalla, G. Surekha, R. P. Suvarna and K. V. Krishnaiah, Gadolinium Nitrate Decorated Reduced Graphene Oxide Structure and Morphological Studies for Battery Applications, *ECS Trans.*, 2022, **107**, 19589.
30 S. R. Ch, R. N. Bulakhe, J. K. R. Modigunta, G. Murali, J. Kim, E. Park, B. Kang, I. In, A. K. Roy and K. Ramakrishnan, Tin oxide/nitrogen-doped graphene quantum dots composite nanotubes: an efficient electrode for supercapacitors, *J. Nanomater.*, 2022, **2022**, 3167809.
31 X. Liu, Z. Lu, X. Huang, J. Bai, C. Li, C. Tu and X. Chen, Self-assembled S, N co-doped reduced graphene oxide/MXene aerogel for both symmetric liquid- and all-solid-state supercapacitors, *J. Power Sources*, 2021, **516**, 230682.
32 Y. Cheng, Y. Zhan, J. Ran, Z. Wang, S. Agnoli, H. Xia and G. Granozzi, Hybrid MXene/reduced graphene oxide aerogel microspheres for hydrogen evolution reaction, *Ionics*, 2021, **27**, 3099–3108.
33 L. Zhang, K. Yu, Y. Li, Z. Wang, K. Zhan, J. Yang and B. Zhao, Nanoparticles of Fe_3O_4 Anchored on $Ti_3C_2T_x$ MXene/rGO Aerogels as Hybrid Negative Electrodes for Advanced Supercapacitors, *ACS Appl. Nano Mater.*, 2022, **6**, 482–491.
34 M. Liu, P. Song, D. Liang, Y. Ding and Q. Wang, 3D porous $Ti_3C_2T_x$ MXene/rGO/SnO_2 aerogel for formaldehyde detection at room temperature, *J. Alloys Compd.*, 2022, **925**, 166664.
35 M. Liu, Z. Wang, P. Song, Z. Yang and Q. Wang, Flexible MXene/rGO/CuO hybrid aerogels for high performance acetone sensing at room temperature, *Sens. Actuators, B*, 2021, **340**, 129946.
36 K. Chaudhary, N. Shaheen, S. Zulfiqar, M. I. Sarwar, M. Suleman, P. O. Agboola, I. Shakir and M. F. Warsi, Binary WO_3-ZnO nanostructures supported rGO ternary nanocomposite for visible light driven photocatalytic degradation of methylene blue, *Synth. Met.*, 2020, **269**, 116526.
37 H. Yang, T. Zhang, M. Jiang, Y. Duan and J. Zhang, Ambient pressure dried graphene aerogels with superelasticity and multifunctionality, *J. Mater. Chem. A*, 2015, **3**, 19268–19272.
38 Z. Cai, Y. Ma, K. Zhao, M. Yun, X. Wang, Z. Tong, M. Wang, J. Suhr, L. Xiao and S. Jia, $Ti_3C_2T_x$ MXene/graphene oxide/Co_3O_4 nanorods aerogels with tunable and broadband electromagnetic wave absorption, *Chem. Eng. J.*, 2023, **462**, 142042.
39 R. Wang, H. Xuan, J. Yang, G. Zhang, Z. Xie, X. Liang, P. Han and Y. Wu, Controllable synthesis of complex nickel-vanadium selenide three dimensional flower-like structures as an attractive battery-type electrode material for high-performance hybrid supercapacitors, *Electrochim. Acta*, 2021, **388**, 138649.
40 G. Vinodha, P. Shima and L. Cindrella, Mesoporous magnetite nanoparticle-decorated graphene oxide nanosheets for efficient electrochemical detection of hydrazine, *J. Mater. Sci.*, 2019, **54**, 4073–4088.
41 M. S. Begum and A. J. Ahamed, Facile Synthesis of NiSe:Zn Nanoparticles by Method Variation and their Morphological Studies, *Chem. Sci.*, 2016, **5**, 472–478.
42 A. K. Singh, N. Shukla, D. K. Verma, B. Kumar, K. Mandal and R. B. Rastogi, Reinforcement of nanoporous lanthanum-doped zinc borate by vanadium selenide nanosheets

for improved tribological activity, *RSC Adv.*, 2022, **12**, 18685–18696.

43 B. Huang, X. Tong, X. Zhang, Q. Feng, M. N. Rumyantseva, J. Prakash and X. Li, MXene/NiO composites for chemiresistive-type room temperature formaldehyde sensor, *Chemosensors*, 2023, **11**, 258.

44 B. C. Ozkan, T. Soganci, H. Turhan and M. Ak, Investigation of rGO and chitosan effects on optical and electrical properties of the conductive polymers for advanced applications, *Electrochim. Acta*, 2019, **295**, 1044–1051.

45 B. Bi, Y. Guan, D. Qiao, X. Chen, M. Bao, Z. Wang and Y. Li, MXene/Graphene modified cellulose aerogel for photo-electro-assisted all-weather cleanup of high-viscous crude oil from spill, *J. Hazard. Mater.*, 2023, **460**, 132353.

46 E. Aliyev, V. Filiz, M. M. Khan, Y. J. Lee, C. Abetz and V. Abetz, Structural characterization of graphene oxide: Surface functional groups and fractionated oxidative debris, *Nanomaterials*, 2019, **9**, 1180.

47 B. Scheibe, K. Tadyszak, M. Jarek, N. Michalak, M. Kempiński, M. Lewandowski, B. Peplińska and K. Chybczyńska, Study on the magnetic properties of differently functionalized multilayered $Ti_3C_2T_x$ MXenes and Ti-Al-C carbides, *Appl. Surf. Sci.*, 2019, **479**, 216–224.

48 K. Chaudhary, B. Basha, S. Zulfiqar, S. Yousaf, E. W. Cochran, M. Al-Buriahi, M. F. Warsi and M. Shahid, 3D cellular lattice like-Ti_3C_2 MXene based aerogels embedded with metal selenides particles for energy storage and water splitting applications, *Fuel*, 2023, **351**, 128856.

49 Y. Li, F. Meng, Y. Mei, H. Wang, Y. Guo, Y. Wang, F. Peng, F. Huang and Z. Zhou, Electrospun generation of $Ti_3C_2T_x$ MXene@graphene oxide hybrid aerogel microspheres for tunable high-performance microwave absorption, *Chem. Eng. J.*, 2020, **391**, 123512.

50 S. Xu, J. Du, J. Li, L. Sun and F. Li, Nickel-selenide templated binary metal–organic frameworks for efficient water oxidation, *J. Mater. Chem. A*, 2020, **8**, 16908–16912.

51 M. Walsh, J. Z. Tan, S. Nagarajan, K. Macgregor, J. M. Andresen, M. M. Maroto-Valer and S. Pitchaimuthu, From brew to clean fuel: harnessing distillery wastewater for electrolysis H_2 generation using nano scale nickle selenide water oxidation catalysts, *Sustainable Energy Fuels*, 2024, **8**, 192–201.

52 S. R. KA, N. Barman, S. Radhakrishnan, R. Thapa and C. S. Rout, Hierarchical architecture of the metallic VTe_2/$Ti_3C_2T_x$ MXene heterostructure for supercapacitor applications, *J. Mater. Chem. A*, 2022, **10**, 23590–23602.

53 A. Ghobadi, T. G. U. Ghobadi, A. K. Okyay and E. Ozbay, Emerging photoluminescence from defective vanadium diselenide nanosheets, *Photonics Res.*, 2018, **6**, 244–253.

54 Z. Li, X. Wang, W. Zhang and S. Yang, Two-dimensional Ti_3C_2@CTAB-Se (MXene) composite cathode material for high-performance rechargeable aluminum batteries, *Chem. Eng. J.*, 2020, **398**, 125679.

55 T. Shang, Z. Lin, C. Qi, X. Liu, P. Li, Y. Tao, Z. Wu, D. Li, P. Simon and Q. H. Yang, 3D macroscopic architectures from self-assembled MXene hydrogels, *Adv. Funct. Mater.*, 2019, **29**, 1903960.

56 Y. Bourlier, M. Bouttemy, O. Patard, P. Gamarra, S. Piotrowicz, J. Vigneron, R. Aubry, S. Delage and A. Etcheberry, Investigation of InAlN layers surface reactivity after thermal annealings: a complete XPS study for HEMT, *ECS J. Solid State Sci. Technol.*, 2018, **7**, P329.

57 M. Jia, Y. Jin, P. Zhao, C. Zhao, M. Jia, L. Wang and X. He, Hollow $NiCoSe_2$ microspheres@N-doped carbon as high-performance pseudocapacitive anode materials for sodium ion batteries, *Electrochim. Acta*, 2019, **310**, 230–239.

58 M. V. Narayana and S. N. Jammalamadaka, Tuning optical properties of graphene oxide under compressive strain using wet ball milling method, *Graphene*, 2016, **5**, 73.

59 W.-D. Yang and Y.-J. Lin, Preparation of rGO/BiO composites by hydrothermal synthesis for supercapacitor electrode, *J. Electr. Eng.*, 2019, **70**, 101–106.

60 T. T. Nguyen, J. Balamurugan, V. Aravindan, N. H. Kim and J. H. Lee, Boosting the energy density of flexible solid-state supercapacitors via both ternary NiV_2Se_4 and $NiFe_2Se_4$ nanosheet arrays, *Chem. Mater.*, 2019, **31**, 4490–4504.

61 L. Antony, E. Pavitra, K. S. Ranjith, G. S. R. Raju, Y. S. Huh and Y.-K. Han, Ag Nanoparticles-Decorated Bimetal Complex Selenide 3D Flowers: A Solar Energy-Driven Flexible Hybrid Supercapacitor for Smart Wearables, *Adv. Fiber Mater.*, 2024, 1–14.

62 Y. Wang, Y. Zhang, R. Shao and Q. Guo, FeSe and Fe_3Se_4 encapsulated in mesoporous carbon for flexible solid-state supercapacitor, *Chem. Eng. J.*, 2022, **442**, 136362.

63 K. Chaudhary, S. Zulfiqar, K. M. Katubi, Z. A. Alrowaili, M. Shahid, M. S. Al-Buriahi, M. F. Warsi and E. W. Cochran, Integration of Polymorphic Co_xSe_y on MXene-Incorporated Self-Templated Three-Dimensional Graphene Foam to Augment Supercapacitor Performance through Componential and Structural Modifications, *ACS Appl. Energy Mater.*, 2024, 1814–1827.

64 X. Wu, Y. Qiu, B. Yang, J. Li, W. Cai, Y. Qin, Y. Kong and Z.-Z. Yin, Fabrication of $CoSe_2$/CoP with rich selenium- and phosphorus-vacancies and heterogeneous interfaces for asymmetric supercapacitors, *J. Colloid Interface Sci.*, 2023, **651**, 128–137.

65 W. Adan, E. W. Cochran, S. Zulfiqar, M. F. Warsi, I. Shakir and K. Chaudhary, Wet-chemical engineering of Ag-$BiVO_4$/Bi_2S_3 heterostructured nanocomposite on graphitic carbon nitride (g-C_3N_4) sheets for high performance supercapacitor application, *J. Energy Storage*, 2023, **72**, 108416.

66 M. Anwar, E. W. Cochran, S. Zulfiqar, M. F. Warsi, I. Shakir and K. Chaudhary, In-situ fabricated copper-holmium co-doped cobalt ferrite nanocomposite with cross-linked graphene as novel electrode material for supercapacitor application, *J. Energy Storage*, 2023, **72**, 108438.

67 J. Zhao, H. Cheng, Z. Zhang, Y. Liu, J. Song, T. Liu, Y. He, A. Meng, C. Sun and M. Hu, The semicoherent interface and vacancy engineering for constructing Ni(Co)Se_2@Co(Ni)Se_2 heterojunction as ultrahigh-rate battery-type supercapacitor cathode, *Adv. Funct. Mater.*, 2022, **32**, 2202063.

68 X. Wu, Z.-B. Zhai, K.-J. Huang, R.-R. Ren and F. Wang, Boosting energy and power performance of aqueous energy storage by engineering ultra-fine metallic VSe_2 nanoparticles anchored reduced graphene oxide, *J. Power Sources*, 2020, **448**, 227399.

69 C. Li, G. Jiang, M. Demir, Y. Sun, R. Wang and T. Liu, Preparation of rGO/MXene@NiCo-P and rGO/MXene@Fe_2O_3 positive and negative composite electrodes for high-performance asymmetric supercapacitors, *J. Energy Storage*, 2022, **56**, 105986.

70 M. Chen, J. Chen, X. Tan, W. Yang, H. Zou and S. Chen, Facile self-assembly of sandwich-like MXene/graphene oxide/nickel–manganese layered double hydroxide nanocomposite for high performance supercapacitor, *J. Energy Storage*, 2021, **44**, 103456.

71 W. Wu, C. Zhao, J. Zhu, D. Niu, D. Wei, C. Wang, F. Wang and L. Wang, Hierarchical materials constructed by 1D hollow nickel–cobalt sulfide nanotubes supported on 2D ultrathin MXenes nanosheets for high-performance supercapacitor, *Ceram. Int.*, 2020, **46**, 12200–12208.

72 J.-F. Hou, J.-F. Gao and L.-B. Kong, A crystalline nickel vanadium oxide@amorphous cobalt boride nanocomposites with enhanced specific capacity for hybrid supercapacitors, *Electrochim. Acta*, 2021, **377**, 138086.

73 B. Shen, X. Hu, H.-T. Ren, H.-K. Peng, B.-C. Shiu, J.-H. Lin, C.-W. Lou and T.-T. Li, Rosette-like (Ni, Co)Se_2@Nb_2CT_x MXene heterostructure with abundant Se vacancies for high-performance flexible supercapacitor electrodes, *Chem. Eng. J.*, 2024, 149440.

74 J. Guo, Y. Zhao, N. Jiang, A. Liu, L. Gao, Y. Li, H. Wang and T. Ma, One-pot synthesis of 2D Ti_3C_2/$Ni_2CO_3(OH)_2$ composite as electrode material with superior capacity and high stability for hybrid supercapacitor, *Electrochim. Acta*, 2018, **292**, 168–179.

75 R. Wang, C. Xu and J.-M. Lee, High performance asymmetric supercapacitors: new NiOOH nanosheet/graphene hydrogels and pure graphene hydrogels, *Nano Energy*, 2016, **19**, 210–221.

76 S. Wang, Y. Song, Y. Ma, Z. Zhu, C. Zhao and C. Zhao, Attaining a high energy density of 106 Wh kg^{-1} for aqueous supercapacitor based on VS_4/rGO/CoS_2@Co electrode, *Chem. Eng. J.*, 2019, **365**, 88–98.

77 H. Yi, H. Wang, Y. Jing, T. Peng, Y. Wang, J. Guo, Q. He, Z. Guo and X. Wang, Advanced asymmetric supercapacitors based on CNT@$Ni(OH)_2$ core–shell composites and 3D graphene networks, *J. Mater. Chem. A*, 2015, **3**, 19545–19555.

78 C. Lu, A. Li, T. Zhai, C. Niu, H. Duan, L. Guo and W. Zhou, Interface design based on Ti_3C_2 MXene atomic layers of advanced battery-type material for supercapacitors, *Energy Storage Mater.*, 2020, **26**, 472–482.

79 J. Ramadoss, A. Sonachalam and M. Govindasamy, Facile synthesis of bi-metal oxide composite on a multilayered $Ti_3C_2T_x$ electrode for enhancing capacitance performance of asymmetric supercapacitor, *J. Energy Storage*, 2024, **85**, 111141.

80 M. Li, W. Liu, J. Ju, L. Xie, Y. Chen and J. Jiang, Exploring the effects of temperature-driven phase transition on supercapacitive performance of cobalt diselenide, *J. Power Sources*, 2022, **541**, 231683.

81 R. Ahmad, N. Iqbal, T. Noor, G. Ali, M. Ali, N. Shahzad and M. A. Raza, Zeolitic imidazolate frameworks derived Co-Zn-nanoporous carbon-sulfide material for supercapacitors, *Electrochim. Acta*, 2022, **404**, 139739.

